VII International Conference on Computational Methods in Marine Engineering
MARINE 2017
M. Visonneau, P. Queutey and D. Le Touzé (Eds)

HIGH FIDELITY NUMERICAL SIMULATIONS OF SHIP AND SUBMARINE HYDRODYNAMICS

MARINE 2017

CHRISTER FUREBY*

* The Swedish Defence Research Agency – FOI
Defence Security Systems Technology
SE 147 25 Tumba, Stockholm, Sweden
e-mail: fureby@foi.se

Key words: Large Eddy Simulation, hybrid RANS-LES, wall-models.

Abstract. This paper discusses the use of wall-modeled LES and hybrid RANS-LES models for the prediction of ship and submarine flows. Results from applied cases are discussed to illustrate the use of these methods for practical problems as well as the differences between methods. The paper then discusses the underlying theories and assumptions of wall-modeled LES and hybrid RANS-LES models. The focus of this presentation is on wall-modeled LES as these methods are theoretically more well-founded than hybrid RANS-LES models. Results from both canonical and building block flows are then presented and discussed in order to provide a more firm and practical foundation for the recommendations for applied use that are provided in the final concluding remarks section.

1 INTRODUCTION

Much of the current understanding of ship hydrodynamics has been obtained through systematic wind tunnel and towing tank experiments and tests in model-scale as well as trials and experiments in full-scale. Systematic and continuous analysis of experimental and test results has developed the current understanding of ship hydrodynamics, and to a significant extent also the advanced hull and propulsor designs now entering production. However, the cost of both model-scale, and in particular full-scale, tests and experiments currently precludes large systematic variation of multiple parameters in order to increase our general knowledge of ship hydrodynamics, and other methods of investigation are necessary. Only recently have Computational Fluid Dynamics (CFD) made its entrance onto the ship hydrodynamic arena, [1-2], as supported by the advancements in scientific computing, and the increasing access to large-scale massively parallel computational platforms needed for rapid turn around of simulations and very large simulations, [3]. The ability to perform a very large number of relatively simple and cheap CFD simulations (with limited details) facilitates automatic hull and propeller optimization, [4], whereas the ability to perform very large CFD simulations (with much detail) enables increased detailed understanding of the flow physics. With improved access to such tools, new experimental challenges are posed, focusing on revealing and quantifying details of the flow in order to validate the CFD models, e.g. [5].

The flow around a ship or submarine hull is dominated by the boundary layer that develops over the hull, but is also influenced by the pressure gradients developing over the bow and the

stern as well as the disturbances caused by appendages, struts, bilge-keels, rudders and the propeller(s). CFD simulations require the volume of interest to be subdivided into control volumes, the size of which represents the flow structures to be resolved by the simulation. For the sake of discussion we consider two ships, a small ship with a length of 50 m, a width of 12 m and draught of 4 m, moving at 10 knots, and a large ship with a length of 300 m, a width of 30 m and draught of 10 m, moving at 30 knots. The *global* Reynolds numbers (measuring the ratio of inertial forces to viscous forces, indicating the level of turbulence) of these ships are $Re_0=v_0L/\nu=2.5\cdot10^8$ and $4.6\cdot10^9$, respectively, in which v_0, L and ν are the speed, hull length and viscosity. At model-scale, the Re_0 numbers are approximately two orders of magnitudes smaller, whereas the *integral* Re number, Re_I, (representative of the most energetic eddy turbulence scales) can be assumed one order of magnitude smaller than Re_0. Based on the present understanding of turbulence, [6-9], the ratio of the integral scales, ℓ_I, to the Kolmogorov scales, ℓ_K, scale with Re_I such that $\ell_I/\ell_K\approx Re_I^{3/4}$, which means that the Kolmogorov scales are $\ell_K\approx0.13$ mm and 0.09 mm, respectively. In Direct Numerical Simulation (DNS) (in which all turbulent scales are resolved), [10], the grid resolution, Δ, should be smaller than ℓ_K, which implies that $\sim2.1\cdot10^{11}$ and $\sim6.6\cdot10^{12}$ surface grid cells are needed to resolve the surface flow. If we assume that the computational domain extends one hull-length away from the hull in all directions, and if geometrical progression is used to expand the cells from the hull to a distance of 10% of the hull length, whereafter uniform cells are used, ~56500 and ~348000 cells are required in the wall-normal direction. All in all, this results in that $\sim1.2\cdot10^{16}$ and $\sim2.3\cdot10^{18}$ grid cells are needed to resolve the computational domains around the hulls. The same type of estimate suggests that $\sim5.0\cdot10^{11}$ and $\sim1.0\cdot10^{13}$ grid cells are required for DNS of the corresponding model-scale hulls. These estimates suggest that DNS is unachievable for both model-scale and full-scale ship and submarine hydrodynamics for some time.

The traditional alternative to DNS is to employ Reynolds Averaged Navier-Stokes (RANS) models, [11-12], which is based on computing the mean (time-averaged or ensemble averaged) flow using models, [12-14], for the whole spectrum of the turbulence. RANS has been successfully used for decades to compute the mean flow around many hull forms, and is also widely used in aerodynamics and other related fields. The main drawbacks of RANS are that it cannot handle large-scale unsteadiness, and that the method is not designed to provide information about unsteady features of the flows or small details of the flows. The grid resolution is primarily dictated by the turbulence model selected, [14], but is usually on the order of $\sim1\cdot10^6$ to $\sim30\cdot10^6$ grid cells for a full-scale ship hull.

An alternative to DNS and RANS is Large Eddy Simulation (LES), [15-20], in which only the large energetic eddy scales are explicitly simulated, using a subgrid model to represent the effects of the small-scale turbulence. If we assume that the Taylor scales, [7-9], should be resolved in LES, an estimate, based on the perception that the Taylor scales gradually reduce to the Kolmogorov scales in the wall-normal direction as the hull is approached (resulting in anisotropic near-wall scales) results in that $\sim5.0\cdot10^{11}$ and $\sim1.0\cdot10^{13}$ grid cells are needed for a *wall-resolved LES* of the full-scale hulls, whereas $\sim1.2\cdot10^8$ and $\sim1.6\cdot10^9$ grid cells are required for *wall-resolved LES* of the model-scale hulls. Wall-resolved LES of full-scale ship flows are thus unfeasible but wall-resolved LES of model-scale ship flows are within reach as demonstrated by Posa & Balares, [21]. Analysis, [22-24], suggests that more than 90% of these grid cells are employed to resolve the gradually decreasing eddy scales in the boundary layer. If it can be assumed that the inner part of the boundary layer is 'enslaved' by the outer part of the boundary layer, and hence to behave in a deterministic manner relative to the outer

part of the boundary layer, a model may be used to replace the explicit simulation of the inner part of the boundary layer. Such a simulation approach will hereafter be referred to as a *wall-modeled* LES in contrast to the wall-resolved LES in which the flow in the whole boundary layer is explicitly simulated. Wall-modeled LES thus has the potential of being able to tackle full-scale ship hydrodynamics with available computational resources without significant decrease in accuracy compared to wall-resolved LES, [25]. A similar approach is hybrid RANS-LES, [26-27], which attempts, using different schemes, to merge RANS in the (inner) attached part of the flow with LES in the (outer) detached part of the flow.

In this review we will discuss and compare DNS, wall-resolved LES, wall-modeled LES, hybrid RANS-LES and RANS in order to increase the understanding and usefulness of these complementary methods. Both applied and canonical flows will be discussed using example references idiosyncratic to the author and his colleagues.

2 TARGET CONFIGURATIONS

Here we discuss major flow features of typical target configurations such as flows around surface ships and submarines at straight-ahead and yaw conditions. These discussions are here based on RANS, hybrid RANS-LES and wall-modeled LES in order to illustrate the spectrum of flow physics features that can be predicted by these methods.

Figure 1 shows the flow around a 1:58 scale model of the KRISO Very Large Crude Carrier (KVLCC2), which in full scale has a length of 320.0 m, a width of 58.0 m, a draught of 20.8 m and a displacement volume of 312622 m^3, originally introduced by Van *et al.*, [28]. Comprehensive experimental data are available, ranging from towing tank measurements, [28-31], to wind tunnel measurements, [32-33]. There are also a significant number of computational studies, [34-37], performed on this hull form using different CFD models. More specifically Petterson *et al*., [37], used this hull form to evaluate RANS, hybrid RANS-LES and wall-modeled LES, and to further elucidate the flow physics at straight ahead conditions and 12° and 30° of drift at global Re numbers of $Re_0=3.70\cdot10^6$ and $4.60\cdot10^6$. The RANS computations were performed with ReFRESCO, [38], using the 2003 version of Menter's SST k-ω model, [39], and block-structured O-O grids with 12.7 Mcells in a large cylindrical computational domain with a normalized wall distance of $y^+<1$. Here, $y^+=u_\tau y/\nu$ is the normalized distance to the wall in which $u_\tau=\tau_w^{1/2}$ is the friction velocity and τ_w the wall shear stress. The hybrid RANS-LES were performed with EDGE, [40], using an algebraic turbulence model based on combining a mixing length RANS model, [16], with the Smagorinsky model, [42]. Unstructured grids with 73.5 Mcells and $y^+<1$ were used. The wall modeled LES were performed with OpenFOAM, [43], using the mixed model, [44], a wall model, and unstructured grids with 121, 194 and 202 Mcells depending on the drift angle, with $y^+\approx10$.

The flow images in figure 1 show the vorticity distributions around the KVLCC2 hull from RANS, hybrid RANS-LES and wall-modeled LES at 0°, 12°, and 30° drift, respectively, in terms of iso-surfaces of the second invariant of the velocity gradient tensor, λ_2. At 0° drift the flow is dominated by the boundary layer over the forebody, parallel mid-section and stern. LES reveals a pair of flat bilge vortices, developing at the bow, extending towards the sides of the hull, whereafter they become unstable and participate in forming the aft-body vortices, not observed in RANS or hybrid RANS-LES. Similar vortex shapes are however observed at the midship cross-section in the experimental results of Lee *et al*., [32]. The flow over the stern is very complex due to the combined influences of geometry, pressure gradient and viscosity,

Compared to the RANS, which only predicts the mean aft-body vortices, the hybrid RANS-LES and the LES predicts a complex vorticity field evolving around the unsteady undulating aft-body vortices containing also Ω-shaped vortices developing sideways to the hull. With gradually increasing drift angle, the flow rapidly becomes more complicated: At 12° drift new vortical systems such as a forebody bilge vortex, a fore-body side vortex, a stern vortex, an aft-body side vortex, an aft-body bilge vortex and aft-body hairpin vortices develops, whereas the aft-body vortices have been combined into the aft-body side vortex on the windward side and the aft-body hairpin vortex on the leeward side. The unsteadiness also becomes more evident as can be observed from the hybrid RANS-LES and the LES predictions. At 30° drift the fore-body bilge vortex, forebody side vortex, aft-body side vortex, aft-body hairpin vortex and the aft-body bilge vortex are very well established. A stern vortex can also be found between the aft-body side vortex on the windward side and the aft-body hairpin vortex on the leeward side. As observed also in the LES of the 12° drift case, oblique bilge vortices are observed aft of the fore-body bilge vortex. From the LES predictions these vertical structures are surrounded by secondary vortical structures resulting from Kelvin-Helmholtz vortices and von-Karman shedding over the fore-body and helical instabilities.

The time-averaged axial velocity profiles in figure 1 compares RANS, hybrid RANS-LES and LES predictions in the propeller plane with experimental data from [32] at 0° drift. The most pronounced feature in the axial velocity distribution is the hook-shaped pattern of low-velocity around the propeller boss and the low-velocity regions on either side of the transom part of the hull. These features are captured by all simulation models, but most accurately by the wall-modeled LES. The RANS and hybrid RANS-LES predictions either overpredict or underpredict the size and strength of these features. The hook-shaped flow pattern results from the counter-rotating after-body vortex pair developing on each side of the tapered part of

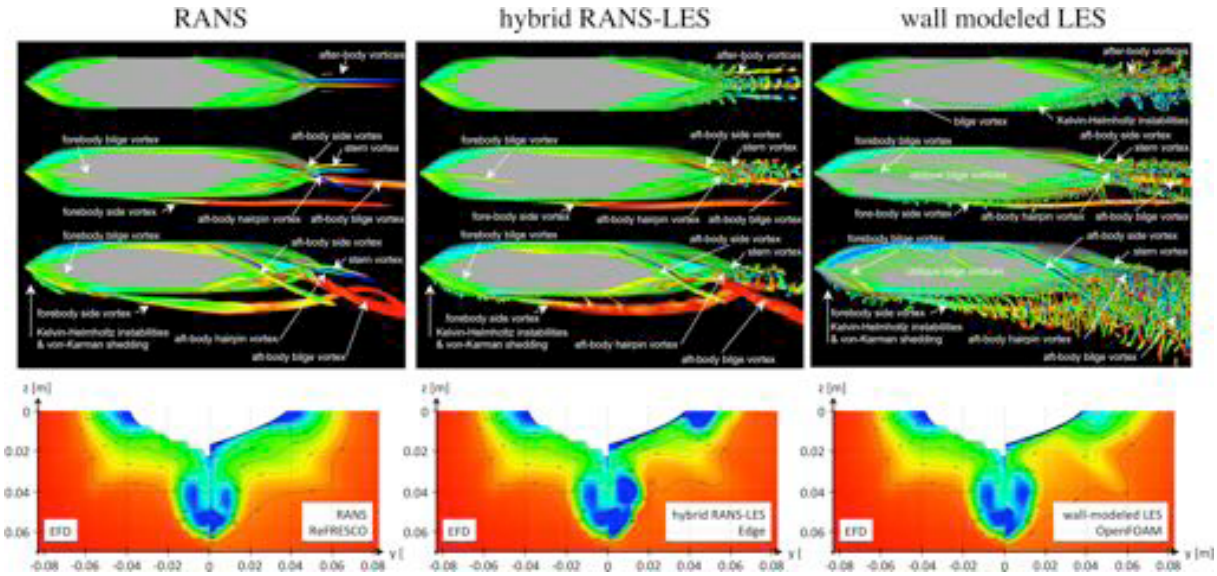

Figure 1: Flow around the KVLCC2 hull in model scale seen from below at 0º drift (top), 12º drift (middle) and 30º drift (bottom). RANS predictions are presented in the left column, hybrid RANS-LES in the middle column, and wall modeled LES in the right column, [37]. In all cases the flow is illustrated using iso-surfaces of the second invariant of the velocity gradient tensor, λ_2. In the three lowest panels the time-averaged axial velocity at 0° drift in the nominal propeller plane is compared with the experimental data from [32].

the lower hull gradually developing over the propeller boss, which in turn is influenced by the low-velocity regions on either side of the stern transom. The low-velocity regions on either side of the stern result from the change in cross-sectional hull area and the large adverse pressure gradient, and gradually thickening boundary layer. This results in the development of the multiple hairpin and Ω-shaped vortex structures found in the LES predictions.

Figure 2 shows the flow around the DSTG Joubert generic submarine model created from the work of Joubert, [45-46], who proposed a design based on principles consistent to achieve low resistance and flow noise, in particular over the forward sonar. The hull-form comprises an axisymmetric body of revolution with a length to diameter ratio of 7.3 and a length of 70.2 m. The bow shape provides a small negative pressure coefficient and pressure gradient, while keeping the location of pressure minima as far aft as possible. Several experimental and computational studies of this hull-form have been conducted, [47-50]. In [47] wind-tunnel experiments were combined with RANS and wall-modeled LES to investigate the flow around the boat in model scale at straight-ahead conditions, whereas in [48] this research was extended to also include effects of yaw. Unstructured grids with between 209 and 340 Mcells were used, with surface averaged y^+ values of ~20. Good agreement between experimental data, comprising surface flow characterization using tufts, pressure distribution along the meridian plane and Particle Imaging Velocimetry (PIV) data in 'stitched' patches at the meridian plane and in

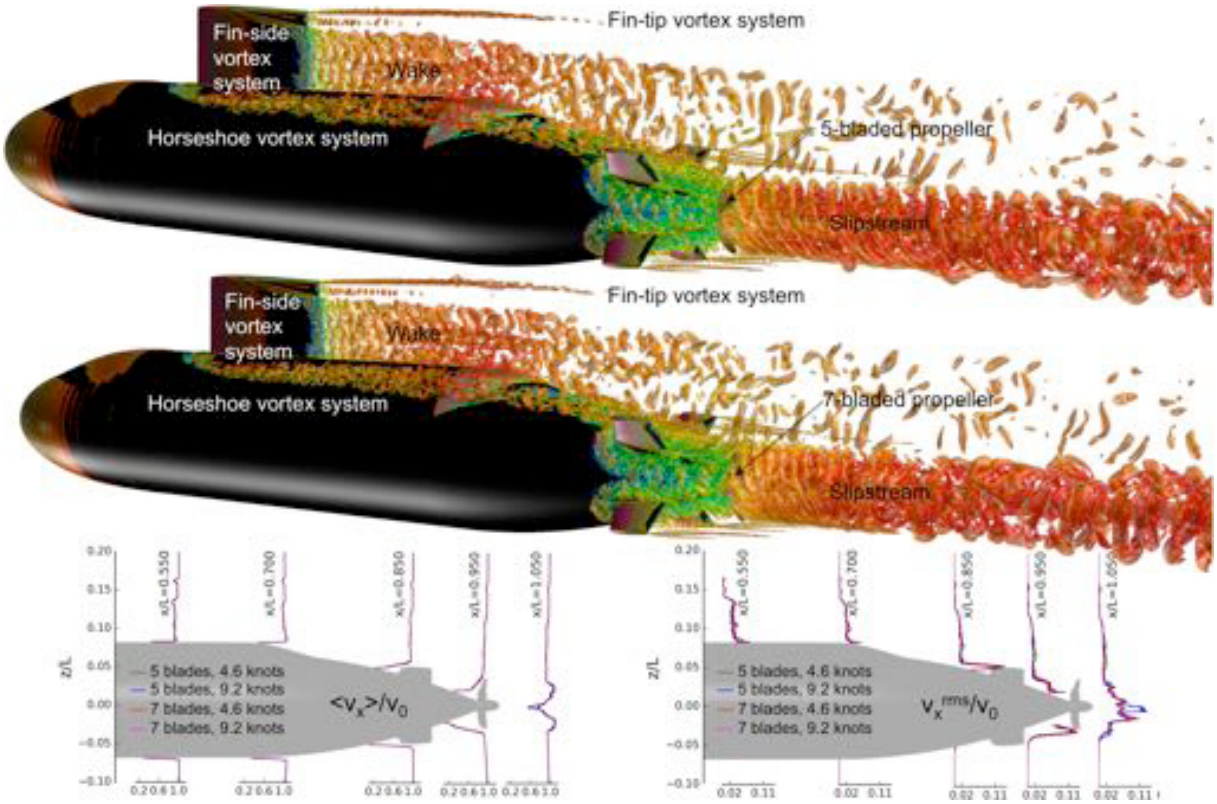

Figure 2: Flow around the fully appended Joubert submarine model in full scale at straight ahead conditions at 9.2 knots with a 5-bladed propeller (top) and a 7-bladed propeller (bottom), [50]. The flow is illustrated with iso-surfaces of the second invariant of the velocity gradient tensor, λ_2. At the two lower panels the time-averaged axial velocity, $\langle v_x \rangle / v_0$, and its rms fluctuations, v_x^{rms}/v_0, are presented in various cross-sections along the hull for the two propeller configurations and for the two boat speeds of 4.6 and 9.2 knots.

several cross-sectional planes, [47-49], and RANS as well as wall-modeled LES were demonstrated. The combined experimental and computational flow predictions provided a comprehensive picture of the flow physics that was summarized in [48]. In [49] this research was further extended to include also propulsion effects. More specifically, numerical simulations using wall-modeled LES were performed for a full-scale version of the DSTG Joubert generic submarine equipped with a 5-bladed propeller (DSTG 115-1) and a 7-bladed propeller (DSTG 057-1), and simulations were performed at two speeds, 4.6 and 9.2 knots. For the wall modeled LES, unstructured grids were employed with between 209 and 309 Mcells, having surface averaged y^+ values of ~100 and ~200 depending on the speed. Particular refinement patches were added in the stern region, around the propeller and in the slipstream.

The top and middle panels of figure 2 show the flow around the full-scale DSTG Joubert generic submarine in terms of iso-surfaces of the second invariant of the velocity gradient tensor, λ_2, colored by the axial velocity. Near the intersection of the fin and the casing, the flow rolls up into a horseshoe-vortex system that surrounds the base of the fin and extends downstream along the casing until it interacts with other vortices in the stern, and with the wake of the fin. Standing side-vortices are formed towards the trailing edge of the fin that interact with the unsteady hull boundary layer and the horseshoe vortex, creating an unsteady wake behind the fin. The flow over the fin-cap is dominated by two sets of vortical structures – a main pair of counter-rotating vortices that develop at the widest section of the fin-cap, separate from the trailing edge of the fin-cap and persist far downstream to the stern region; and a secondary pair consisting of a vortex on each side of the fin just below the cap. This secondary pair is seen to separate from the trailing edge of the fin, below the fin cap, and continue downstream with a small deviation towards the casing. In contrast, the primary vortex pair appears to deviate away from the casing as they travel downstream. Towards the stern, the legs of the horseshoe vortex system pass between the upper rudders whilst interacting with the innermost leg of the horseshoe- vortex system developing around the upper rudders. Additional horseshoe-vortex systems develop around the lower rudders. Tip vortices are shed from the propeller blades and are seen to persist for a number of propeller diameters until they gradually break-up. A central vortex extending downstream of the hub is also produced by the propeller and maintains its form much further aft than the blade-tip vortices.

The two bottom panels of figure 2 compare the predictions of the time-averaged axial velocity, $\langle v_x \rangle / v_0$, and the axial rms velocity fluctuations, v_x^{rms}/v_0, at some axial locations from x/L=0.550 to x/L=1.105. Included in the comparisons are all four wall-modeled LES predictions with both propeller configurations at both boat speeds. Regarding $\langle v_x \rangle / v_0$, it is seen that the velocity is virtually unaffected by the choice of propeller and only marginally influenced by the speed. The boundary-layer development and the gradually weakening imprints of the fin-tip vortex pair and secondary fin-tip vortex system are not affected by either the propeller or the speed. Even the time-averaged flow over the stern appears almost unaffected by the choice of propeller. The $\langle v_x \rangle / v_0$ distribution across the slipstream, however, reveals that that 5-bladed DSTG115-1 propeller results in a more intense hub-vortex. Regarding v_x^{rms}/v_0, elevated fluctuation levels are observed in the wake behind the fin and in the hull boundary layer. Along the tapered stern part of the hull, the region of high velocity fluctuations gradually widens as the horseshoe vortex structures interact with the boundary layer. Only small differences in v_x^{rms}/v_0 can be observed along the stern, but v_x^{rms}/v_0 increases with increasing speed. Moreover, the stronger tip vortex of the 5-bladed DSTG115-1 propeller also results in higher levels of v_x^{rms}/v_0 that stretches far downstream in the slipstream.

3 MATHEMATICAL MODELING

Next, we will outline the frameworks involved in the mathematical modeling of turbulent flows in general and near-wall flows in particular. This modeling survey will be brief, and for details of different methods and implementations we refer to the original papers.

3.1 Governing Equations, DNS, LES, Hybrid RANS-LES and RANS

Irrespectively of modeling approach, DNS, wall-resolved LES, wall-modeled LES, hybrid RANS-LES or RANS, the governing equations are the Navier-Stokes equations,

$$\partial_t(\mathbf{v})+\nabla\cdot(\mathbf{v}\otimes\mathbf{v})=-\nabla p+\nabla\cdot\mathbf{S},\ \nabla\cdot\mathbf{v}=0, \tag{1}$$

in which $\mathbf{v}$ is the velocity, $\mathbf{S}=2\nu\mathbf{D}$ the rate of strain tensor, ν the viscosity, and $\mathbf{D}=\frac{1}{2}(\nabla\mathbf{v}+\nabla\mathbf{v}^T)$ the rate of strain tensor, in which $\nabla\mathbf{v}$ is the velocity gradient tensor.

In RANS the Navier-Stokes equations (1) are averaged over an ensemble of equivalent flows, $\langle\mathbf{v}\rangle(\mathbf{x})=\frac{1}{N}\Sigma_{i=1}^{N}\mathbf{v}^{(N)}(\mathbf{x},t)$, or equivalently over time, $\langle\mathbf{v}\rangle(\mathbf{x},t)=\int_T\mathbf{v}(\mathbf{x},t)dt$, so that,

$$\partial_t(\langle\mathbf{v}\rangle)+\nabla\cdot(\langle\mathbf{v}\rangle\otimes\langle\mathbf{v}\rangle)=-\nabla\langle p\rangle+\nabla\cdot(\langle\mathbf{S}\rangle-\mathbf{R}),\ \nabla\cdot\langle\mathbf{v}\rangle=0, \tag{2}$$

in which $\mathbf{R}=\langle\mathbf{v}'\otimes\mathbf{v}'\rangle$ is the Reynolds stress tensor, representing the transport of momentum due to the velocity fluctuations $\mathbf{v}'$. In order to close (2) and to represent the effects of the turbulence, $\mathbf{R}$ must be modeled. A common method of approximating the $\mathbf{R}$ is based on the hypothesis that the effects of turbulence are analogous to an increased viscosity. This is justifiable when effects such as energy dissipation and increased mass transport normal to mean flow streamlines are considered. The Boussinesq relationship, [51], between the Reynolds stresses and the mean flow strain embodies this approximation and is formulated as $\mathbf{R}=-2\nu_t\langle\mathbf{D}\rangle_D$, in which ν_t is the turbulent viscosity and $\langle\mathbf{D}\rangle$ the mean rate-of-strain tensor. Many different closure models for $\mathbf{R}$ are available, [12, 52], including algebraic, one-equation, two-equation and differential stress equation models. The most widely used RANS turbulence models are the k-ε model, [53, 12], in which $\nu_t=c_\mu k^2/\varepsilon$, and the Shear Stress Transport (SST) k-ω model, [39], in which $\nu_t=a_1k/\max(a_1\omega, F_2|\langle\mathbf{D}\rangle||)$. Here, k is the turbulent kinetic energy, ε the dissipation rate, and ω the specific dissipation rate, all of which are obtained from modeled transport equations. For further details we refer to [12, 39, 52-53]. Most of these models are available in two versions: one for use with grids that have a wall-normal resolution of $y^+\leq1$, and one for use with grids that have a wall-normal resolution of $y^+>30$, and then in conjunction with a RANS wall-model, [52], that relates the wall shear stress, τ_w, to the mean or time-averaged velocity $\langle\mathbf{v}\rangle$ adjacent to the wall, using additional physical relationships.

In wall-resolved and wall-modeled LES, the Navier-Stokes equations (1) are low-pass filtered, [15], using a convolution operator of the form $\bar{\mathbf{v}}(\mathbf{x},t)=G_\Delta*\mathbf{v}=\int_D G_\Delta(\mathbf{x}-\mathbf{x}',\Delta)\mathbf{v}(\mathbf{x}',t)d^3\mathbf{x}'$ to remove the small subgrid scales (assumed more universal), [15-19], so that,

$$\partial_t(\bar{\mathbf{v}})+\nabla\cdot(\bar{\mathbf{v}}\otimes\bar{\mathbf{v}})=-\nabla\bar{p}+\nabla\cdot(\bar{\mathbf{S}}-\mathbf{B}),\ \nabla\cdot\bar{\mathbf{v}}=0, \tag{3}$$

in which $\mathbf{B}=(\overline{\mathbf{v}\otimes\mathbf{v}}-\bar{\mathbf{v}}\otimes\bar{\mathbf{v}})$ is the subgrid stress tensor, representing unresolved transport of momentum on the resolved flow, [15-19]. In order to close (3) and to represent the physics of the unresolved flow, $\mathbf{B}$ must be modeled. According to Sagaut, [15], models for $\mathbf{B}$ can generally

be divided into *functional* and *structural* models depending on if they are indented to mimic the kinetic energy cascade from large to small eddy scales, usually assumed to be of inertial sub-range character, or if they are intended to mimic the structure of the subgrid flow physics. A wide variety of LES subgrid models are available, and Sagaut, [15], provides a comprehensive summary and review of these two model classes. Functional models are more frequently used than structural models, and are also generally more robust, since most functional models are based on a Boussinesq relationship, so that $\mathbf{B}=-2\nu_k\bar{\mathbf{D}}$, in which ν_k is the subgrid viscosity. A wide range of subgrid viscosity models are available including algebraic models such as the well-known Smagorinsky (SMG) model, the Wall-Adapting Local Eddy (WALE), and the σ-model, as well as one-equation models such as the One Equation Eddy Viscosity (OEEVM) model and the Localized Dynamic k-equation Model (LDKM). For further details we refer to [15] and references therein. Note that whereas wall-resolved LES only need the subgrid models, wall-modeled LES typically need additional models to represent the near-wall flow physics that is not explicitly resolved on the grid. The modeling of the near-wall flow physics in wall-modeled LES is significantly more challenging than in RANS since in LES we are resolving a significant part of the unsteady eddy motion in the boundary layer, and particularly in the outer part of the boundary layer where the flow is more energetic.

RANS have been successful in simulating wall bounded flows for decades, providing, however, only the mean velocity, $\langle\mathbf{v}\rangle$, and the modeled turbulent stresses, $\mathbf{R}$, whereas LES, providing instantaneous flow realizations of the resolved velocity, $\bar{\mathbf{v}}$, as well as any statistical moment of $\bar{\mathbf{v}}$, have been considered too expensive for practical applications unless used with a wall model. Wall-modeled LES have been less-well understood and is questioned due to the additional complexity of modeling only a fraction of the near wall flow physics, whereas the remaining fraction of the near wall flow physics is resolved on the grid. As an alternative, the class of hybrid RANS-LES has evolved in which the attached flow is treated by RANS and the detached flow is treated by LES, [14, 26-27], and references therein. Hybrid RANS-LES suffers from the well-known issues of how to unambiguously define the attached and detached flow regions and how to create grids that support both RANS and LES in the two regions, as well as the transition between these two regions, [26-27]. Improved understanding of the flow physics as well as the governing equations have resulted in improved hybrid RANS-LES models that better handle different grid topologies and inappropriate grid resolution. An issue not discussed is that of how the governing hybrid RANS-LES equations are formulated: That both the RANS and LES equations (2) and (3), respectively, have the same mathematical appearance is thus taken as a basis for the hybrid RANS-LES equations,

$$\partial_t(\tilde{\mathbf{v}})+\nabla\cdot(\tilde{\mathbf{v}}\otimes\tilde{\mathbf{v}})=-\nabla\tilde{p}+\nabla\cdot(\tilde{\mathbf{S}}-\mathbf{T}),\ \nabla\cdot\tilde{\mathbf{v}}=0, \tag{4}$$

in which $\mathbf{T}=(\widetilde{\mathbf{v}\otimes\mathbf{v}}-\tilde{\mathbf{v}}\otimes\tilde{\mathbf{v}})$ is the hybrid RANS-LES stress tensor. The bridge between the LES and RANS formulations can be expressed by the definition of the hybrid RANS-LES variables $\tilde{\mathbf{v}}(\mathbf{x},t)=(G_\Delta\circ G_T)*\mathbf{v}(\mathbf{x},t)=\int_T\int_D G(\mathbf{x}-\mathbf{x}',\Delta)\mathbf{v}(\mathbf{x}',t)d^3\mathbf{x}'dt$, in which $G_\Delta\circ G_T$ is a spatio-temporal filter kernel that may be able to distinguish between attached (or RANS) flow regions, in which $\tilde{\mathbf{v}}(\mathbf{x},t)=G_T*\mathbf{v}=\langle\mathbf{v}\rangle(\mathbf{x},t)$, and detached (or LES) flow regions, in which $\tilde{\mathbf{v}}(\mathbf{x},t)=G_\Delta*\mathbf{v}=\bar{\mathbf{v}}(\mathbf{x},t)$. Two conceptually different hybrid RANS-LES model types are commonly referred to: The first approach can be divided into two branches in which the first branch is based on Speziale's, [54], ideas that $\mathbf{T}=f_\Delta(\Delta/\ell_K)\mathbf{R}$, in which any RANS turbulence model, $\mathbf{R}$, can be used, and $f_\Delta(\Delta/\ell_K)$ is the contribution function, the role of which is to damp the contribution of $\mathbf{R}$, since part of

the turbulence is resolved in the regime where the solution becomes unsteady. One suggested contribution function, [53], is $f_\Delta(\Delta/\ell_K)=(1-\exp(-\beta\Delta/\ell_K)^n$, in which $\beta=0.001$ and $n=1$. The second branch is based on a weighted sum of LES and RANS models so that for eddy-viscosity and subgrid viscosity models, the hybrid RANS-LES stress tensor is $\mathbf{T}=-2\nu_{hRL}\tilde{\mathbf{D}}$, in which the hybrid RANS-LES viscosity is $\nu_{hRL}=\psi\nu_t+(1-\psi)\nu_k$, in which ν_t is the RANS eddy-viscosity, ν_k the LES subgrid viscosity, and ψ the blending factor. In this approach any RANS turbulence and LES subgrid viscosity model can be used. Typically, the blending factor depends on different solution dependent parameters from the RANS and LES models including the filter width, Δ, and the distance to the wall, d. The second approach in commonly referred to as Detached Eddy Simulation (DES), [14, 26-27], and is based on a unified approach in which the same model is used both for the attached (RANS) and detached (LES) flow regions. The discriminating factor is that the distance, d, to the wall is typically replaced by a simple switch function of the form $\tilde{d}=\min\{d, c_{DES}\Delta\}$. Close to the wall, where $d<c_{DES}\Delta$, the model utilize the original RANS model. Away from the wall, were $d>c_{DES}\Delta$, the model turns into a subgrid model. The original formulation is based on the Spalart-Allmaras model, [55], that turns into the well-known Smagorinsky subgrid model, [15], in the limit of LES.

3.2 Near-Wall Flow Physics

The general understanding of a turbulent boundary layer has been known since the 1950's and it is composed of virtually chaotic fluid motion that results in pressure fluctuations at the wall surface. Figure 3 is a schematic of a turbulent boundary layer that shows the irregular division between the turbulent and freestream flow and the flattened shape of the mean velocity as a function of the distance from the wall, [56]. It is generally assumed that the pressure and velocity fluctuations disappear outside of the intermittent edge of the boundary layer. Experimental data and DNS predictions agree on that the boundary layer can be divided into an *inner layer*, which in turn is composed of a *viscous sub-layer*, dominated by viscous stresses, a *buffer layer*, in which both viscous and turbulent stresses are important, and a *log-law region*, which is dominated by turbulent stresses, and an *outer layer*, which is dominated by the external flow and the large-scale turbulence, [57]. As evident from the visualizations in [57], the turbulence kinetic energy is primarily carried by eddies of different characteristic sizes in the different layers near and far from the wall. This reveals that the turbulent boundary layer is a multi-scale phenomenon that any form of modeling needs to respect.

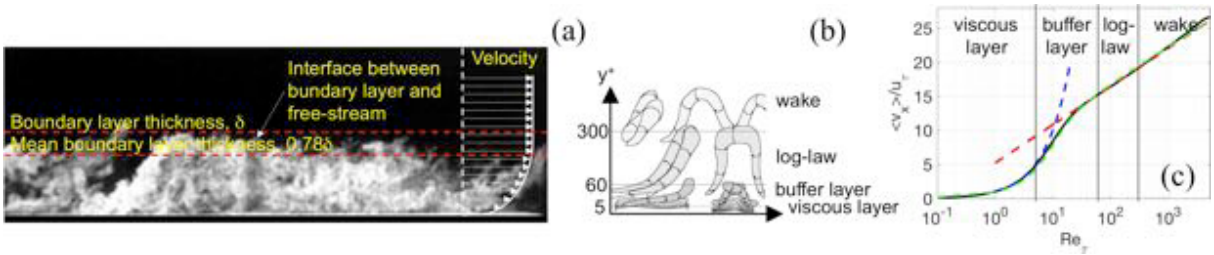

Figure 3: Flow physics in a turbulent boundary layer: (a) experimental visualization, (b) schematic of the coherent structure topology and (c) layers, and velocity profiles. Legend: (—) DNS data from fully developed turbulent channel flow, [58], (—) analytical solution to the ensemble averaged Navier-Stokes equations in the viscous sublayer ($0<y^+<5$) (5), (—) analytical solution to the ensemble averaged Navier-Stokes equations in the log-law region ($60<y^+<300$) (7) and finally (—) Spalding's law of the wall (8), [59].

The key aspects of turbulent boundary layers are most easily explained using the ensemble averaged incompressible Navier-Stokes equations (2). For the viscous sublayer, $y^+<5$, equation (2) simplifies to $\nu\partial^2\langle v_x\rangle/\partial y^2=\partial\langle p\rangle/\partial x$. By integrating this equation twice with respect to y, assuming that $\partial\langle p\rangle/\partial x$ is independent of y, and after introducing the wall-shear stress component, $\tau_w=\nu(\partial\langle v_x\rangle/\partial y)|_w$, and the normalized streamwise velocity, $v_x^+=\langle v_x\rangle/u_\tau$, and wall distance, $y^+=u_\tau y/\nu$, with $u_\tau=\tau_w^{1/2}$ being the friction velocity, we obtain that,

$$v_x^+=y^+ +\frac{\nu}{2u_\tau^3}\frac{\partial\langle p\rangle}{\partial x}(y^+)^2. \tag{5}$$

For the log-law region, $60<y^+<300$, equation (1) becomes $\partial R_{xy}/\partial y=-\partial\langle p\rangle/\partial x$, By integrating this equation with respect to y, assuming that $\partial\langle p\rangle/\partial x$ is independent of y, and moreover that $R_{xy}=-\nu_t(\partial\langle v_x\rangle/\partial y)$, in which the turbulent viscosity is modeled as $\nu_t\approx\kappa u_\tau y$, with κ being the von-Karman constant, we obtain, after rearrangement and the subsequent introduction of the non- normalized velocity $v_x^+=\langle v_x\rangle/u_\tau$ and wall distance $y^+=u_\tau y/\nu$, that,

$$\frac{\partial v_x^+}{\partial y^+}=\frac{1}{\kappa y^+}+\frac{\nu}{\kappa u_\tau^3}\frac{\partial\langle p\rangle}{\partial x}. \tag{6}$$

By integrating equation (6) we finally obtain that,

$$v_x^+=\frac{1}{\kappa}\ln(y^+)+\frac{\nu}{\kappa u_\tau^3}\frac{\partial\langle p\rangle}{\partial x}y^+ +B. \tag{7}$$

For a zero pressure-gradient boundary layer the von-Karman constant is $\kappa\approx0.41$, whereas $B\approx 5.2$. In the intermediate buffer-layer, $5<y^+<60$, the flow physics dominating the viscous sublayer gradually transitions into the flow physics dominating the inertial sub-layer, and hence no analytical model exists for this layer. Figure 3 shows a typical turbulent boundary layer velocity profile in which the viscous and log-law regions are presented as dashed lines together with the well-known Spalding's law-of-the-wall curve fit, [59],

$$y^+=v_P^+ +e^{-(\kappa B)}[e^{(\kappa v_P^+)}-[1-(\kappa v_P^+)-\tfrac{1}{2!}(\kappa v_P^+)^2-\tfrac{1}{3!}(\kappa v_P^+)^3+\ldots]], \tag{8}$$

designed using experimental data to provide a continuous velocity profile through a zero pressure gradient boundary layer. The continuous velocity profile (8) asymptotically agrees with (5), when $\partial\langle p\rangle/\partial x=0$, in the viscous sub-layer and (7) in the log-law region, and thus provides a foundation for developing a deterministic model of the near wall flow.

3.3 Wall-Modeled LES

The philosophy of wall-modeled LES is to respect the multi-scale nature of the boundary layer, by directly resolving the energetic eddies in the outer layer (where they are large) but to model the energetic eddies in the inner layer (where they are small). As a consequence of this, the inner-layer dynamics (streaks, quasi-streamwise vortices, peak production and dissipation, etc.) is completely or partly removed from the dynamical system explicitly computed and represented by a single value of the wall shear stress, τ_w, that the models is supposed to provide.

This is a severe truncation of the wall-turbulence dynamical system – as it has to be in order to drastically reduce the computational cost – and since the model is also required to handle a situation where parts of the inner-layer dynamics is resolved, the model needs to be very flexible and be able to take a passive role compared to the evolution of the resolved flow structures. Given the removal of the peak production region in the inner layer (typically occurring at $y^+\approx12$) turbulence can no longer be produced in the modeled boundary layer, and thus all resolved outer-layer turbulence needs to be produced (and later dissipated) in the outer layer, as expected in high-Re wall-turbulence, where the Reynolds stresses have been found to be predominantly produced at the same wall distance as they are later dissipated, [60].

At a first glance this understanding of wall-modeled LES also incorporates hybrid RANS-LES models. There is, however, an important and discriminating distinction between wall-modeled LES and hybrid RANS-LES models in that for wall-modeled LES the LES equations (3) apply all the way down to the wall, whereas for hybrid RANS-LES models the LES equations (3) apply only above a certain 'interface' y_{int} (which may be defined implicitly, but nevertheless exists) below which the RANS equations (2) apply. The distinction between hybrid RANS-LES and wall-modeled LES is subtle but important: In wall-modeled LES, a wall-model is used to estimate τ_w but the coupling between the LES and wall-model is rather weak: the LES feeds velocity data to the wall-model at $y=h_{wm}$, and the wall-model feeds wall-shear-stress data back to the LES at $y=0$. Apart from this, no other information is exchanged. Notably, while the LES could impart flow structures onto the wall-model, the ability of flow structures in the wall-model to enter the LES region is limited. Perhaps more importantly, the formal definition of the LES equations applying all the way down to the wall implies that the LES equations and the wall-model overlap for a distance of h_{wm}.

Two different types of wall modeled LES are currently employed: one-equation and algebraic. In one-equation wall-models, [61-62], the thin boundary layer equations, [12],

$$\frac{\partial}{\partial y}[(\nu+\nu_t)\frac{\partial \overline{v}_x}{\partial y}]=0 \quad \text{with} \quad \nu_t=\kappa y u_\tau(1-\exp(y^+/A^+)^2, \tag{9}$$

in which $A^+\approx17$, are solved on an auxiliary one-dimensional wall-normal grid extending away from the wall into the LES domain. Equation (9) is solved over the region $0\leq y\leq h_{wm}$, using a no-slip condition at the wall, $y=0$, and with v_x equal to the LES wall-parallel velocity, $\overline{v}_{//}$, at $y=h_{wm}$. The wall-shear stress τ_w from the wall-model (9) is computed from $\tau_w=\nu(\partial v_x/\partial y)|_w$. The next step is to construct the full wall-shear stress vector $\boldsymbol{\tau}_w$ by assuming that it is aligned with the velocity parallel to the wall, and by using a simple linear approximation for the wall-normal velocity (for the wall-normal stress). The final step is to couple this back to the LES equations (3) which is often done by using $\boldsymbol{\tau}_w$ as a boundary condition for the LES momentum equation. In algebraic wall-models, [63], an even simpler procedure is followed, using Spalding's law-of-the-wall. Given the LES velocity in the grid cells adjacent to the wall, $\overline{v}_P$, the friction velocity, u_τ, and hence also the wall-shear stress, τ_w, are computed by solving (8), in which v_P^+ is substituted for $\overline{v}_P/u_\tau$, for each grid cells adjacent to the wall,

$$y^+=\overline{v}_P/u_\tau+e^{-(\kappa B)}[e^{(\kappa\overline{v}_P/u_\tau)}-[1-(\kappa\overline{v}_P/u_\tau)-\tfrac{1}{2!}(\kappa\overline{v}_P/u_\tau)^2-\tfrac{1}{3!}(\kappa\overline{v}_P/u_\tau)^3+\ldots]]. \tag{10}$$

The next step is to construct the full wall-shear stress vector $\boldsymbol{\tau}_w$ by assuming that it is aligned with the velocity parallel to the wall, and by using a simple linear approximation for the wall-

normal velocity (for the wall-normal stress). The final step is to couple this back to the LES equations (3) which can be done by using $\boldsymbol{\tau}_w$ as a boundary condition for the LES momentum equation or by modifying the viscosity at the wall, [63], by introducing a wall-viscosity, ν_{BC} such that $\tau_w=u_\tau^2=\nu(\partial v_x/\partial y)|_w\approx(\nu+\nu_{BC})(\overline{v}_P/y_P)$, which can be inverted to give the value for the effective viscosity $\nu+\nu_{BC}$ at the wall, $\nu+\nu_{BC}=u_\tau^2 y_P/\overline{v}_P=u_\tau y_P/v_P^+$.

It is important to note the 'input-output' character of the wall-model irrespectively of it being of one-equation or algebraic nature. The wall-model takes information from the LES in the form of instantaneous data at grid points some distance above the wall and returns the wall shear stress or friction velocity to the LES at the wall, y=0. This data is then used by the LES to construct approximate boundary conditions at the wall, y=0.

Figure 4 attempts to illustrate the principal differences between wall-resolved LES, the two main branches of wall-modeled LES, algebraic and one-equation, and hybrid RANS-LES. For wall-resolved LES the main challenge is to create a computational grid that is sufficiently fine everywhere to resolve the Taylor scales, $\ell_T\approx v'/(\varepsilon/\nu)^{1/2}$, in which ε is the dissipation rate and $v'=k^{1/2}$ the velocity fluctuations. When the wall is approached the Taylor scales gradually decrease in size until they approach the Kolmogorov scales, $\ell_K=(\nu^3/\varepsilon)^{1/4}$, which are the smallest scales in turbulence. From the definition of the Taylor and Kolmogorov scales if follows that $\ell_T\approx\ell_I/Re_I^{1/2}$ and $\ell_K\approx\ell_I/Re_I^{3/4}$, which in turn implies that $\ell_T/\ell_K\approx Re_I^{1/4}$, from which we may conclude that the characteristic scales become highly anisotropic, with aspect ratios of between 50 and 200 for high Re number flows, as the wall is approached. DNS results and experimental data indeed reveal that the near-wall flow is highly anisotropic, being dominated by large-scale high- and low-speed streaks aligned with the flow, being ~1000(ν/u_τ) long, and having a spacing of ~100(ν/u_τ), in which (ν/u_τ) is the viscous length-scale in the boundary layer. Around these streaks we have vortex structures that are aligned with the streaks for some distance until they rise to form part of Ω-shaped structures of different sizes. High-speed fluid, *sweeps*, moves from the outer part of the boundary layer into the inner part of the boundary layer and, conversely, low-speed fluid, *ejections*, moves from the inner to the outer part of the boundary layer. A wall-resolved LES have no problems capturing these features as showed for example for a turbulent pipe flow at Re_τ=1000, [64]. Here, a grid of 589 Mcells was required for the DNS whereas a grid of only 36 Mcells was required for the wall-resolved LES. The difference

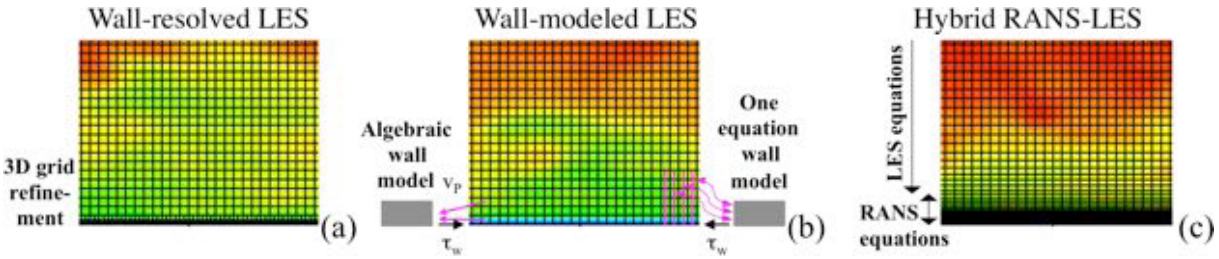

Figure 4: The principles of (a) wall-resolved LES, (b) wall-modeled LES using algebraic wall-models (left) and one-equation wall-models (right) and (c) hybrid RANS-LES. The background is from wall-resolved, wall-modeled and hybrid RANS-LES simulations of fully developed turbulent channel flow at Re_τ=1000. The different grid systems are superimposed on the LES velocity predictions.

in skin friction between the DNS and LES predictions in comparison to hot-wire anemometry data were 1.7% and 5.2%, respectively, whereas the differences in boundary layer and momentum thickness, and shape factor were smaller. For wall-resolved LES it may be advanta-

geous to use unstructured grids with hanging nodes as illustrated in figure 4a to concentrate the grid resolution to the inner part of the boundary layer.

The two main branches of wall-modeled LES are illustrated in the left and right panels of figure 4b, respectively. In both cases, the LES grid is comparatively coarse in the wall normal direction, which significantly reduces the overall computational cost, but relies on a model to represent the physics in the inner part of the boundary layer and to some extent also the physics in the outer part of the boundary layer. The fact that these models work with both resolved and unresolved flow physics data makes their interactions with the underlying LES flow more complicated. The remedy to this issue is to make sure that there is an overlap region in which both the resolved LES fields and the wall-model are active and exchange information. Regarding the grid resolution in wall-resolved LES we anticipate a conventional LES grid with cell sizes of the size of the Taylor scales, as often assumed to the most appropriate cell size for an LES, all the way to the wall, also in the wall normal direction. Since the boundary layer flow physics is generally described in terms of viscous length scales, $\ell_V=\nu/u_\tau$, which can be converted to Taylor scales, $\ell_V=(\nu'/u_\tau)\ell_T$, the streaks (~$1000\ell_V$ long, having a spacing of ~$100\ell_V$ and a radius of ~$5\ell_V$) are generally rather well resolved in a wall-resolved LES with a grid spacing of $O(\ell_T)$. It is, however, the smallest scales and flow structures associated with the velocity gradient and the viscosity at the wall, residing in the viscous sub-layer and in the buffer layer, that need to be explicitly handled by the wall-model.

Regarding the hybrid RANS-LES illustrated in figure 4c the interface between the RANS and LES regimes is allowed to vary depending on how the flow develops. Regarding the grid, it is determined in principle by the implicit requirement of the RANS model, usually requesting that $y^+\leq 1$, typically resulting in a grid that is extensively stretched towards the wall, resulting in flat, sheet-like grid cells at the wall. Most hybrid RANS-LES models suffer from some degree of problem in maintaining the correct mean velocity profile around the interface. Most often, the mean velocity $v^+(y^+)$ in the LES region ends up above the log-law, and thus this is called the "log-layer mismatch". Multiple studies have reported improvements that can remove the log-layer mismatch, through either the addition of small-scale forcing or by tailoring the blending function between the RANS and LES eddy-viscosities. The caveat, however, is that the results depend quite strongly on the forcing amplitude, [65].

4 CANONICAL FLOW CASES

In order understand more about the RANS, DES and LES models we next summarize the application of these models to a few relevant canonical flow cases.

4.1 Fully Developed Turbulent Channel Flow

Fully developed turbulent channel flow is a simple canonical building block flow that has been examined using RANS, DES, LES and DNS for decades, e.g. [58, 66-69]. The channel is typically confined between two parallel plates, 2h apart, where h is the channel half-width. The flow is driven by a mass flow in the axial (e_x) direction, no-slip conditions are applied in the cross-stream (e_y) direction, and periodic conditions are applied in the spanwise (e_z) direction. Here, results will be discussed for Re_τ=550 and 1000, 2000 and 5200, following the DNS of Lee & Moser, [58]. The channel used is 9h×2h×4h in the axial, wall-normal and spanwise directions, respectively. For wall-resolved LES the grid is designed with $\Delta x=\Delta y=\Delta z\approx 0.0333\cdot h$ in the core of the channel, whereas in the near-wall region, $y<0.0333\cdot h$, the grid is uniformly

refined in all three directions so that $y^+\approx1$. For the different Re_τ numbers, this strategy results in grids of 4.21, 11.47, 40.50 and 152.5 Mcells, respectively. For wall-modeled LES the grid is designed so that $\Delta x=\Delta y=\Delta z\approx0.0333\cdot h$ in the whole channel, resulting in 1.94 Mcells, and y^+ values of 9, 16, 32 and 84, respectively, for the different Re_τ numbers. For DES, the grid is designed with $\Delta x=\Delta y=\Delta z\approx0.0333\cdot h$ in the core of the channel, whereas in the near-wall region, $y<0.0333\cdot h$, stretching is applied in the wall normal direction so that $y^+\approx1$ at the wall, resulting in between 2.65 and 3.88 Mcells depending on Re_τ.

The upper and lower panels of figure 6a show perspective views of the flow in the channel from wall-modeled LES using the LDKM model, [15], and wall-resolved LES using the WALE model, [15], at $Re_\tau=2000$, in terms of contours of the axial velocity, $\overline{v}_x$, and the friction velocity, u_τ, at the lower wall, and iso-surfaces of the second invariant, λ_2, of the velocity gradient tensor, $\nabla\mathbf{v}$. For both the wall-resolved and wall-modeled LES the λ_2-iso-surfaces reveal a plethora of different vortical structures: Streamwise vortices, forming an acute angle with the wall, are observed to agglomerate in the low-speed streaks, and hairpin vortices, rapidly bending away from the wall, form due to shear between the low-speed and high-speed streaks. Thinner, mainly streamwise, vortical structures are located in the wall-resolved LES between and beneath the low-speed and high-speed streaks. The streaks are $\sim1000\cdot\nu/u_\tau$ long, having a spacing of $\sim100\cdot\nu/u_\tau$, and the hairpin vortices have a diameter of between 2 and $10\cdot\nu/u_\tau$. The wall-modeled LES cannot resolve the vortical structures between and beneath the streaks, but resolves the streaks as well as the largest (and strongest) hairpin vortices.

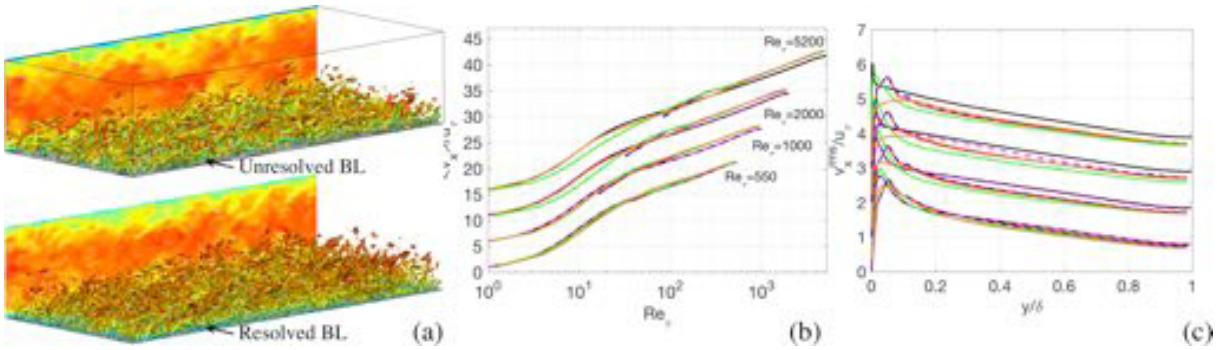

Figure 5: Fully developed turbulent channel flow. In (a) results from wall-modeled (top) and wall-resolved bottom) LES at $Re_\tau=2000$ are presented in terms of λ_2. In (b) and (c) profiles of the time-averaged axial velocity, $\langle v_x\rangle$, and its rms fluctuations, v_x^{rms}, are presented for $Re_\tau=550$, 1000, 2000 and 5200, respectively. Legend: (—) DNS, [58], (—) *wall-resolved* LES using the LDKM model, (—) *wall-modeled* LES using the WALE model, (—) *wall-modeled* LES using the LDKM model, (—) hybrid RANS-LES using the DES model, [14], and (—) hybrid RANS-LES using the IDDES model, [26-27].

Figures 5b and 5c compare the mean streamwise velocity, $\langle v_x\rangle$, and the streamwise rms-velocity fluctuations, $v_x^{rms}=\sqrt{\langle(v_x-\langle v_x\rangle)^2\rangle}$, normalized with u_τ, from DNS, [58], wall-resolved LES, using the WALE subgrid models, wall-modeled LES, using the WALE and LDKM subgrid models, DES, [14], and IDDES, [26-27]. For $\langle v_x\rangle$ we find excellent agreement between DNS and wall-resolved LES for $Re_\tau=550$, 1000 and 2000, with no existing LES for $Re_\tau=5200$. The wall-modeled LES present very good agreement with the DNS given the coarse grids in the near-wall region. Virtually no difference is noted between the WALE and LDKM subgrid models. For DES and IDDES we find that IDDES performs better than DES, and both models

show good agreement across the whole range of Re_τ numbers. Evidence of the 'log-layer mismatch' can however be detected in the DES, IDDES and wall-modeled LES. For v_x^{rms} we find good agreement between the DNS and the wall-resolved LES, whereas the wall-modeled LES predicts a peak in v_x^{rms} at the first grid point instead of at $y^+\approx12$ due to the coarse grid. Apart from that, the agreement is satisfactory. For the DES and IDDES results we find that both of these methods fail to predict v_x^{rms} in the core flow, and IDDES also undrerpredicts the peaks in v_x^{rms}. For the wall-resolved LES the error in skin-friction, C_f, is ~2% at Re_τ=5200. For the wall-modeled LES, DES and IDDES the error in C_f, is between 5% and 9%.

4.2 Zero Pressure Gradient Flat Plate Boundary Layer Flow

The next level of complexity is facilitated by the flow over a flat plat at zero pressure gradient. Historically, knowledge of flat plate turbulent boundary layers was gained experimentally, [70-72], but more recently have DNS, [73-74], and LES, [75-76], also significantly contributed to the current level of understanding of boundary layers. Spatially developing boundary layer simulations are typically set up in a rectilinear computational domain as illustrated in figure 6a. Here, a computational domain is set-up to emulate the experimental study of De-Graaf & Eaton, [72], and the DNS of Schlatter & Örlü, [74]. The domain is 2.00 m long, 0.20 m wide and 0.127 m high, and is discretized with hexahedral cells having cell sizes of Δx=2.6 mm, Δy=0.80 mm and Δz=2.00 mm, resulting in a baseline grid of 12.16 Mcells. A uniformly refined grid with 97.28 million cells has been used to study the statistical grid convergence. No-slip boundary conditions are applied at the wall, periodic boundary conditions are applied in the spanwise direction, whereas open inflow/outflow boundary conditions are applied at the inlet and outlet, respectively. RANS, with the SST k-ω model, wall-modeled LES, with the WALE and LDKM models, and hybrid RANS-LES, with the DES and IDDES models, have here be-en performed. The LES are provided with a numerical trip, 20 mm downstream of the inlet, at ~Re_θ=100, to stimulate the boundary layer development.

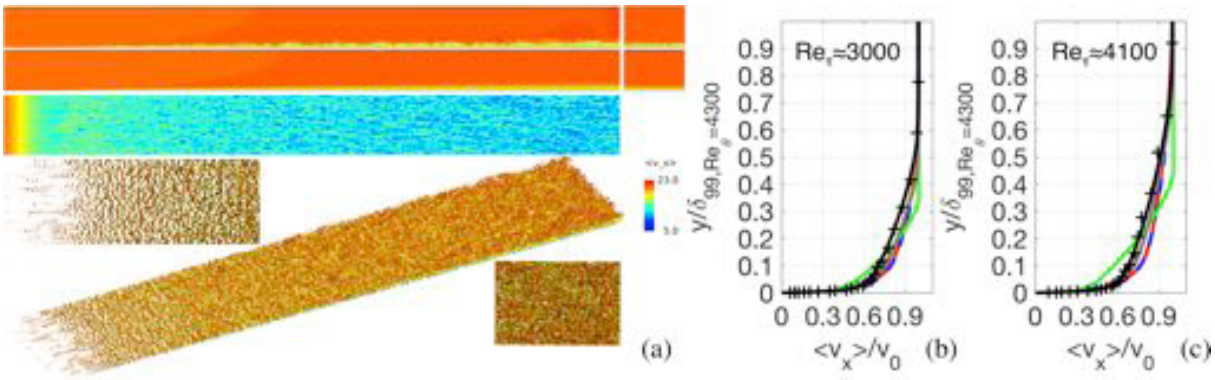

Figure 6: Zero Pressure Gradient Flat Plate Boundary Layer flow. In (a) results from wall-modeled LES are presented in terms of λ_2, instantaneous and time-averaged velocity contours, $\bar{v}_x$ and $\langle v_x \rangle$, and friction velocity, u_τ, contours, and in (b) and (c) normalized axial velocity profiles, $\langle v_x \rangle$, are compared for $Re_\tau\approx2900$ and 5200, respectively. Legend: (×) experimental data, [72], (—) DNS, [74], (—) *wall-modeled* LES using the WALE model, (—) *wall-modeled* LES using the LDKM model, (—) hybrid RANS-LES using the DES model, (—) hybrid RANS-LES using the IDDES model, and (—) RANS using the SST k-ω model.

In figure 6a we present a few selected views of the flat plate boundary layer flow in terms

of instantaneous and time-averaged axial velocities, v_x, and $\langle v_x \rangle$, wall-friction velocities, u_τ, and iso-surfaces of the second invariant of the velocity gradient tensor, $\nabla \mathbf{v}$, from the wall-modeled LES with the LDKM model on the baseline grid. All simulations result in boundary layers that thicken with downstream distance from the leading edge approximately according to $\delta \simeq 0.16x/Re_x^{1/7} \simeq 0.16x^{6/7}(\nu/v_0)^{1/7}$, [70]. The boundary layers predicted by the LES models are all populated by a plethora of vortices, developing downstream of the numerical trip, whereas those predicted by the DES and IDDES seem virtually free of vortical structures. In the LES, the disturbances created by the numerical trips gradually develop into coherent vortical structures in which the streamwise vorticies, forming an acute angle with the wall, agglomerate in the low-speed streaks, and hairpin vorticies, rapidly bending away from the wall, form due to shear between the low-speed and high-speed streaks. The vortices resolved in the wall-modeled LES are typically thicker than those resolved in the target DNS, but reveal the same topology and dynamic behavior as the target DNS. This behavior is similar to the so-called 'fat worms' observed in LES of homogeneous isotropic turbulence, [77].

Figures 6b and 6c present time-averaged axial velocity profiles, $\langle \overline{v}_x \rangle$, normalized by the freestream velocity, v_0, at two different locations corresponding to momentum thickness Re-numbers of $Re_\theta \simeq 3030$ and 4060, respectively. The boundary layer thickens with downstream distance from the leading edge, as observed in the experimental data from deGraaff & Eaton, [72], and from the DNS of Schlatter & Örlu, [74], and it is apparent that the RANS SST-kω prediction captures this behavior very well. The DES model underpredicts the growth rate of the boundary layer, and predicts a more laminar like profile along the whole flat plate. The IDDES models predict a boundary layer in agreement with the experimental and DNS data. The wall-resolved LES, using the WALE and LDKM subgrid models, respectively, show virtually indistinguishable boundary layer profiles in reasonable agreement with the experimental and DNS data but with a somewhat broader and fuller $\langle \overline{v}_x \rangle$-profile.

5 INTERMEDIATE COMPLEXITY FLOW CASES

To further enhance the understanding of the RANS, DES and LES models we summarize the application of these models to a few selected flow cases of higher geometrical and induced physical complexity relevant to marine or offshore interest.

5.1 Flow around a 3D Bump

The next case considered is the flow over a 3D hill attached to a rectilinear wind tunnel section, [78-80]. The experiment feature a h=0.078 m high 3D axisymmetric hill mounted on the floor of a H=0.25 m high wind tunnel. The inlet speed is v_0=27.5 m/s giving a Re number, based on h, of Re≈143,000. The wind tunnel test section is 7.62 m long and 3.03 m wide, and the hill is analytically defined, [78]. LES of this flow have been performed by e.g. Patel & Menon, [81], Persson *et al*., [82], Visbal & Risetta, [83], and Garcia-Villalba *et al*., [84], and RANS have been performed by several researchers as summarized in [85]. Different computational domains are used by different investigators but as illustrated in figure 7a two approaches prevail: short domains using pre-curser channel flow simulations, [84], and simulations of the whole test section of the wind tunnel, [82], to model the boundary layer evolution. The grids used in [81-85] range from 4.0 to 134.5 Mcells, and the objectives of these computations are also different as explained in the references. Here, we will compare the wall-resolved LES of Garcia-Villalba *et al*., [84], with wall-modeled LES, using the LDKM and WALE subgrid

models, and RANS using the SST-k-ω model. Open inflow/outflow boundary conditions are used at the in- and outlets, respectively, no-slip boundary conditions are used at the upper and lower channel walls and slip conditions are applied in the spanwise direction.

The flow over and around the 3D hill is very complicated as explained in all the references cited, and as also seen from figure 7b, showing instantaneous iso-surfaces of the second invariant of the velocity gradient tensor, λ_2, colored by the velocity, v_x. As the boundary layer approaches the 3D hill, the pressure increases but the increase is not large enough to cause separation. As the flow accelerates over the top of the hill the pressure decreases. Minimum pressure occurs at the top, and is followed by an adverse pressure gradient at the lee-side of the hill, which results in complex flow separation and reattachment in the shallow wake of the hill. Oil-flow visualization and skin-friction visualizations from the LES shows that the separation and reattachment is very complicated with multiple unsteady vortical structures. These flow structures result as a consequence of the acceleration over the top and around the sides of the hill due to the favorable pressure gradients in both directions. The spanwise favorable pressure gradient in front of the hill causes the flow to diverge outward, however, at the lee-side this gradient becomes adverse, causing the side boundary layers to converge on the back of the hill and closer to the center plane in a high-pressure region. The presence of the 3D hill modifies the vorticity distribution, primarily through the pressure gradients, and results in a wake that is inhabited by hairpin-vortices that are deformed by the high level of resolved and subgrid turbulence in the wake behind the 3D hill.

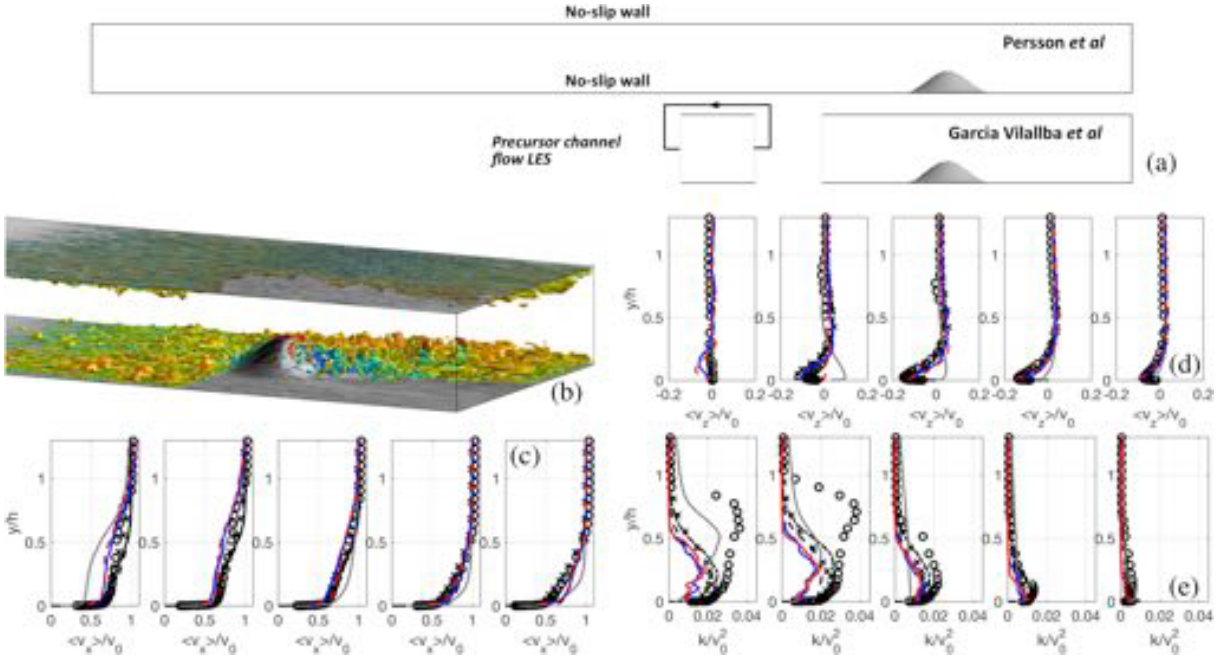

Figure 7: Flow around a 3D bump. In (a) different computational set-ups are presented, (b) results from wall-modeled LES in terms of λ_2, and in (c), (d) and (e) normalized velocity and turbulence profiles, $\langle v_x \rangle$, $\langle v_z \rangle$ and k, respectively, are compared. Legend: (×) experimental data, [79], (○) experimental data, [80], (—) *wall-resolved* LES using the DSMG model, [84], (—) *wall-modeled* LES using the WALE model, (—) *wall-modeled* LES using the LDKM model and (—) RANS using the SST k-ω model.

Figures 7c to 7e show normalized and time-averaged streamwise, $\langle v_x \rangle$, and cross-stream,

$\langle v_z \rangle$, velocity profiles, together with profiles of the turbulent kinetic energy, k. Experimental data from LDV of Byun & Simpson, [79], and hot-wire of Ma & Simpson, [80], are included together with wall-resolved LES predictions of Garcia-Villalba *et al*., [84], and wall-modeled LES predictions, using the LDKM and WALE subgrid models, together with RANS predictions, using the SST k-ω model. The first observation is the similarity of the two experimental velocity data sets, and the difference in the corresponding k data sets. This is due to the difference in measurement technique employed, and highlight the complexity of performing accurate flow measurements of complex cases. The RANS predictions do not capture the essential features of the flow, resulting in poor predictions of both $\langle v_x \rangle$, $\langle v_z \rangle$ and k. The RANS results are good representatives of what may be expected from modern RANS as may be observed by comparing also with other RANS results in [85]. The wall-resolved LES, [84], show extremely good agreement with both experimental velocity data sets, and with the hot-wire experimental data set for k, supporting the use of hot-wire anemometry. The two wall-modeled LES predictions show very similar results, with only minor variations due to choice of subgrid model, that also agrees favorably with the wall-resolved LES, [84], and both experimental velocity data sets, and with the hot-wire experimental data set for k.

5.2 Flow around a Generic Bare Hull Submarine Configuration

The final case considered is the flow around the bare-hull version of the DSTG Joubert generic submarine model created from the work of Joubert, [45-46], and discussed in more detail in [47]. The model have an overall length of 1.35 m, a length to diameter ratio of 7.3, and consists of a cylindrical mid-body, an ellipsoid bow and a parabolic stern, figure 8a. Representative of modern submarine shapes, this generic test article has no full-scale equivalent. The model was experimentally tested in the DSTO low speed wind tunnel, [86], in the octagonal test section of which it was mounted using a floor-mounted pylon with a shrouded fairing. The experimental testing was boundary layer tripping devices, which consisted of either a circular wire of diameter 0.2 mm or 0.5 mm, or a 3 mm wide circumferential strip of distributed silicon carbide grit of size 80, [47]. The trip was located at an axial coordinate of x=67.5 mm measured from the nose of the hull, which corresponds to $x/L \approx 0.05$. Moreover, the location of the trip was positioned far enough upstream to ensure it did not experience an adverse pressure gradient, which under such conditions could lead to undesirable separation, and far enough downstream to ensure the boundary layer would not relaminarize. The overall blockage ratio for the model at zero-incidence was estimated to be about 2.2%. The model was equipped with flush mounted static pressure tappings along the top centerline of the hull in order to estimate the mean pressure coefficient C_P, whereas the mean turbulent skin-friction coefficients, C_f, was measured using the Preston tube method, [87]. The velocity around the upper part of the stern section was measured with Particale Imaging Velocimetry (PIV) in two patches shown in figure 8a. These two patches are stitched together to provide a complete description of the stern flow. Some influence of the mounting was observed. The experimental Re number, based on the hull length and freestream velocity was $5.4 \cdot 10^6$.

Simulations of this case with RANS, using the SST-k-ω model, hybrid RANS-LES, using the DES and IDDES models, and wall-modeled LES, using the WALE and LDKM models, have been performed. Hexahedral grids with 17.0 Mcells, [47], and unstructured grids with 44 and 126 Mcells have been used. No-slip boundary conditions are applied on the hull, whereas conventional freestream and open inflow-outflow boundary conditions are used at the outer

computational boundaries. The freestream turbulence was estimated to 3% in the RANS, DES and IDDES as measured in the wind-tunnel, whereas in LES no freestream turbulence was included. In the IDDES and LES, a numerical trip model was included to model the effects of the trip wire or trip grit used in the wind-tunnel experiments.

Figure 6b shows the vorticity distribution over the hull in terms of iso-surfaces of the second invariant of the velocity gradient tensor, ∇v, denoted λ_2, from the wall-modeled LES using the LDKM model. The iso-surfaces of λ_2 clearly the presence of the numerical trip, befor which the boundary layer is laminar, and after which a turbulent boundary layer gradually develops. The boundary layer remains turbulent along the whole parallel midsection of the hull, and towards the tapered stern an adverse pressure gradient assists in thickening the boundary layer. The LES models as well as the RANS models predict an attached boundary layer all the way to the stern tip. The λ_2 structures of which the boundary layer is composed consists initially of azimuthal disturbances that gradually breaks up to develop a carpet of hairpin-type vortices, the legs of which forms an acute angle to the hull, whereas the neck rises sharply as it bends sideways to connect with is companion forming on the other side of the high-speed or low-speed streak. The hairpin vortex elements are thicker than anticipated, but they behave in the expected way, and so this behavior can be similar to the so-called 'fat worms' observed in the spatially developing boundary layer of Section 4.2, and also in early LES of homogeneous isotropic turbulence as described by Ashurst *et al*., [77]. Along the tapered stern cone, in the thickening boundary layer, the cross-wise momentum transfer creates streamwise vortices that are transported down behind the hull and into the gradually developing wake.

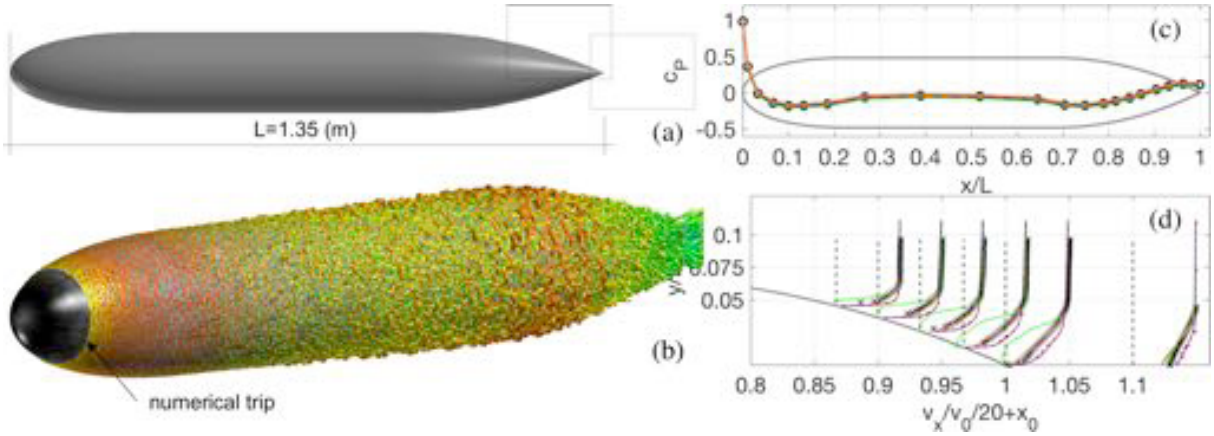

Figure 8: Flow around the DSTG Joubert generic bare-hull submarine configuration. In (a) the hull-shape is outlined together with the PIV patches. In (b) results from wall-modeled LES, using the LDKM model, is presented in terms of λ_2 colored by the streamwise velocity v_x, and in (c) and (d), comparisons of C_P and $\langle v_x \rangle$ are presented. Legend: (×) experimental data, [47], (—) *wall-modeled* LES using the WALE model, (—) *wall-modeled* LES using the LDKM model, (—) hybrid RANS-LES using the DES model, (—) hybrid RANS-LES using the IDDES model, and (—) RANS using the SST k-ω model.

Figure 6c compares the time-averaged or mean static pressure coefficient, C_P. The agreement between the experimental C_P-profile and the computed profiles from the RANS, hybrid RANS-LES and LES predictions is very good along the whole hull. Note that the C_P-profile from the SST-k-ω RANS model is hidden beneath the other profiles. Virtually no difference at all can be observed between the two wall-modelled LES predictions, whereas some minor

differences an be observed between the DES and IDDES models. Figure 6d compares streamwise time averaged or mean velocity profiles in the stern, at x/L=0.867, 0.900, 0.933, 0.967, 1.000 and 1.100, normalized by the freestream velocity v_0. Over the stern-most part of the tail cone, between x/L=0.867 and 1.000, the IDDES and, in particular, the RANS SST-k-ω model predictions show very good agreement with the measurement data. The differences between the RANS SST-k-ω and IDDES model predictions and the PIV data are certainly within the accuracy of the PIV. The DES predictions predict the occurrence of a separation bubble over the stern-most part of the tail cone, not observed experimentally or in any of the simulations, which suggests that this model may be substantially in error. The two wall-modelled LES results are virtually indistinguishable, and seems to predict somewhat too full velocity profiles, and hence slightly too thin boundary layers as also observed in the case of the spatially evolving boundary layer in Section 4.2. The reason for this may very well lie in the details of the numerical trip or in the absence of freestream turbulence, which will interact with the boundary layer turbulence developing over the hull.

6 CONCLUDING REMARKS

High-fidelity (LES and hybrid RANS-LES) numerical simulations of ship and submarine hydrodynamics have reached a certain level of maturity, yet there are still obstacles to overcome before these methods become an everyday tool in marine engineering. The central challenge is the very high Re number encountered in ship- and submarine hydrodynamics, and how to manage the associated issue of an extensive range of eddy scales, ranging from the size of the large eddies of the hull to the smallest Kolmogorov scales. The eddy scales associated with the hull can be O(1) m whereas the associated Kolmogorov scales, representing dissipation of turbulence into heat, can be O(10) mm. The intermediate Taylor scales, at which viscosity affects the turbulence dynamics, can be O(1) mm. This extreme range of scales makes DNS unfeasible for both full-scale and model scale applications. The alternative of RANS have been successfully used for decades to compute the mean flow around numerous hull forms, and is also widely used in aerodynamics and other related fields. The major drawbacks of RANS are that it cannot handle large-scale unsteadiness, and that the method is not designed to provide information about unsteady features of the flows or small details of the flows. This essentially leaves the two branches of wall-resolved and wall-modeled LES, as well as hybrid RANS-LES, as the main candidates for practical ship and submarine flow simulations. These methods are typically required when accurate predictions are needed that also include information about dynamic features such as pressure and turbulence fluctuations that may influence flow noise and vibrations. Wall-resolved LES is however found to be too expensive for today's computational architectures with respect to full-scale predictions, whereas predications of model-scale hull forms are now just manageable.

This leaves wall-modeled LES and hybrid RANS-LES as the only currently feasible candidates for high-fidelity ship and submarine hydrodynamics. The use of any of these methods is not entirely straightforward, and requires substantial knowledge about the methodology as well as some background information about the flow to be computed. This background information can be obtained by RANS and is usually employed to generate computational grids well suited for the two methods of wall-modeled LES and hybrid RANS-LES. Different wall-modeled LES and hybrid RANS-LES models are available but the underlying principles are the same irrespectively of which model is used. Hybrid RANS-LES requires a computational

grid that switches, seamlessly, from an LES grid in the detached flow to a RANS grid in the attached flow. Wall-modeled LES requires an LES grid throughout the whole computational domain. Hybrid RANS-LES relay on an interface, explicit or implicit, to determine when to switch from LES to RANS, whereas wall-modeled LES is based on solving the LES equations all the way to the wall. A wall-model is used just adjacent to the wall to estimate the wall-shear stress (or the friction velocity) from the LES solution in order to provide a boundary condition for the wall-modeled LES.

The flow predictions used to illustrate different aspects of ship and submarine flow physics clearly points at some lack of understanding of high Re number turbulent boundary layers developing over curved and complex surfaces. More high-quality experimental data as well as DNS simulation results are needed to fill the gaps in our current understanding of the boundary layer flow physics, Not until this gap has decreased, improved simulation models, based on the underlying physics can be developed. It is anticipated that such simulation models will be of multi-scale nature, [88], to reflect the multi-scale nature of the boundary layer. The continuous development of algorithms and hardware will help in rapidly reaching higher and thus more relevant Re number flows which are likely to reveal new physical challenges in terms of new physical mechanisms for the composition of a turbulent boundary layer.

ACKNOWLEDGEMENT

The author acknowledges the generous supply of simulation results and many valuable discussions and comments from Brendon Andersson, Daniel Norrison, William Sidebottom, David Clarke, David Jones, Matteo Giacobello, Peter Manovski, Simon Henbest, Ivan Marusic, Myoungkyu Lee, Magnus Tormalm, Suresh Menon, Serge Toxopeus, Fernando Grinstein, Rickard Bensow, Mattias Johansson, Kristian Petterson and Mattias Liefvendal.

REFERENCES

[1] Gorski J.J., 2002, "Present State of Numerical Ship Hydrodynamics and Validation Experiments", ASME J. Offshore Mechanics and Arctin Engng., **124**, p 74.

[2] Stern F., Yang J., Wang Z., Sadat-Hosseini H., Mousaviraad M., Bhushan S. & Xing T.; 2013, "Computational Ship Hydrodynamics: Nowadays and Way Forward", Int. Shipbuilding Prog., **60**, p 3.

[3] Slotnick J., Khodadoust A., Khodadoust J., Darmofal D., Gropp W., Lurie E. & Mavriplis D.; 2013, "CFD Vision 2030 Study: A Path to Revolutionary Computational Aerosciences", NASA Vision 2030 CFD Code Contract NNL08AA16B, Task NNL12AD05T.

[4] Campana E., Peri D., Tahara Y. & Stern F.; 2006, "Shape Optimization in Ship Hydrodynamics using Computational Fluid Dynamics", Comp. Methods Appl. Mech. Engrg., **196**, p 634.

[5] Longo J., Shao J., Irvine M. & Stern F.; 2007, "Phase-Averaged PIV for the Nominal Wake of a Surface Ship
in Regular Head Waves", ASME J. Fluids Engng., **129**, p 524.

[6] Monin A.S.& Yaglom A.M.; 1971. "Statistical Fluid Mechanics: Mechanics of Turbulence", Vol. 2, MIT Press, Cambridge, MA, USA.

[7] Tennekes H. & Lumly J.L.; 1990, "A first Course in Turbulence", MIT press 13th printing.

[8] Frisch U.; 1995, "Turbulence: The Legacy of A.N. Kolmogorov", Cambridge University Press

[9] Tsinober A.; 2009, "An Informal Conceptual Introduction to Turbulence", Springer, **483**.

[10] Kurien S. & Taylor M.A.; 2005, "Direct Numerical Simulations of Turbulence", Los Alamos Science, **29**.

[11] Alfonsi G.; 2009, "Reynolds-Averaged Navier–Stokes Equations for Turbulence Modeling", ASME Appl. Mech. Rev., **62**, p 040802.

[12] Pope, S.B.; 2000, "Turbulent Flows", Cambridge University Press.

[13] Durbin P.A. & Pettersson Reif B.A.; 2010, "Reynolds Averaged Navier–Stokes Equations", In Statistical Theory and Modeling for Turbulent Flows, John Wiley & Sons, Ltd, Chichester, UK.
[14] Spalart P.R.; 2000, "Strategies for Turbulence Modelling and Simulations", Int. J. Heat and Fluid Flow, **21**, p 252.
[15] Sagaut P.; 2001, "Large Eddy Simulation for Incompressible Flows", Springer, Berlin/Heidelberg.
[16] Pope S.B.; 2004, "Ten Questions Concerning the Large-Eddy Simulation of Tturbulent Flows". New J. Phys. **6**, p 35.
[17] Grinstein F.F., Margolin L. & Rider B., (Eds), 2007, "Implicit Large Eddy Simulation: Computing Turbulent Fluid Dynamics", Cambridge University Press.
[18] Georgiadis N.J., Rizetta D.P. & Fureby C.; 2010, "Large Eddy Simulation: Current Capabilities, Recommended Practices, and Future Research", AIAA.J., **48**, p 1772
[19] Piomelli U.; 2015, "Large Eddy Simulations in 2030 and Beyond", Phil. Trans. R. Soc. A **372**, p 20130320.
[20] Fureby C.; 2017, "Challenges for Large Eddy Simulation of Engineering Flows", In Whither Turbulence and Big Data in the 21st Century? p 375, Ed. Pollard A. Castillo L., Danaila L. & Glauser M., Springer Int. Publ.
[21] Posa A. & Balaras E.; 2016, "Large-Eddy Simulations of the DARPA SUBOFF Model in Towed and Propelled Configurations", 31st Symp. on Naval Hydrodynamics, Monteray, USA.
[22] Chapman D.R.; 1979, "Computational Aerodynamics Development and Outlook", AIAA. J, 17, p 1293.
[23] Choi H. & Moin P.; 2012, "Grid-Point Requirements for Large-Eddy Simulation: Chapman's Estimates Revisited". Phys. Fluids, **24**, 011702.
[24] Liefvendahl M., Fureby C. & Boelens O.J.; 2016, "Grid Requirements for LES of Ship Hydrodynamics in Model and Full Scale", 31st Symp. on Naval Hydrodynamics, Monterey, California, USA.
[25] Larsson J., Kawai S., Bodart J. & Bermejo-Moreno I.; 2016, "Large Eddy Simulation with Modeled Wall-Stress: Recent Progress and Future Directions", Mech. Engng. Rev., **3**, p 1.
[26] Spalart P.R., Deck S., Shur M.L., Squires K.D., Strelets M.Kh. & Travin A.K.; 2006, "A New Version of Detached-Eddy Simulation, Resistant to Ambiguous Grid Densities", Theor. Comp. Fluid Dyn., **20**, p 181.
[27] Shur M.L., Spalart P.R. & Strelets M.Kh.; 2008, "A Hybrid RANS-LES Approach with Delayed-DES and Wall-Modelled LES Capabilities", Int. J. Heat & Fluid Flow, **29**, p 1638.
[28] Van S.H., Yim G.T., Kim W.J., Kim D.H., Yoon H.S. & Eom J.Y.; 1997, "Measurement of Flows around 3600 TEU Container Ship Model", Proc. Annual Autumn Meetings, Korea, p 300.
[29] Kume K., Hasegawa J., Tsukada Y., Fujisawa J., Fukasawa R. & Hinatsu M.; 2006, "Measurements of Hydrodynamic Forces, Surface Pressure and Wake for Obliquely Towed Tanker Model and Uncertainty Analysis for CFD Validation", J. Marine Science and Technology, **11**, p 65.
[30] Campana E., Fabbri L. & Simonsen C.D.; 2011, "An Experimental Study of the Water Depth Effects on the KVLCC2 tanker", NATO RTO AVT-189 Specialists Meeting on Assessment of Stability and Control Prediction Methods for NATO Air and Sea Vehicles, RTO-MP-AVT-189-9, Portsdown West, UK.
[31] Kim W.-J., Van S.-H. & Kim D.H.; 2001, "Measurement of Flows around Modern Commercial Ship Models", Exp. Fluids, **31**, p 567.
[32] Lee S.-J., Kim H.-R., Kim W.-J., & Van S.-H.; 2003, "Wind Tunnel Tests on Flow Characteristics of the KRISO 3,600 TEU Containership and 300k VLCC Double-Deck Ship Models", J. Ship Research, **47**, p 24.
[33] Abdel-Maksoud M., Müller, V., Xing T., Toxopeus S., Stern F., Petterson K., Kim S., Eloot K., Gietz U., Schiller P. & Rung, T.; 2015, "Reliable Prediction of Separated Flow Onset and Progression for Air and Sea Vehicles", Chapter 7, Experimental and Numerical Investigations on Flow Characteristics of the KVLCC2 at 30° Drift Angle. NATO AVT-183 Report.
[34] Xing T., Bhushan S. & Stern F.; 2012, "Vortical and Turbulent Structures for KVLCC2 at Drift angle 0, 12, and 30 Degrees", Ocean Engineering, **55**, p 23.
[35] Kim W.J., Kim D.H. & Van S.H.; 2002, "Computational Study on Turbulent Flows around Modern Tanker Hull Forms", Int. J. Num. Methods in Fluids, **38**, p 377.
[36] Turnock S.R., Phillips A.B. & Furlong M.; 2008, "URANS Simulations of Static Drift and Dynamic Maneuvers of the KVLCC2 Tanker", Proc. SIMMAN Workshop, Copenhagen.

[37] Petterson K., Tormalm M., Fureby C. & Toxopeus S.; 2014, "A Computational Study of the flow around the KVLCC2 Model Hull at Straight Ahead Conditions and at 30° Yaw", Ocean Engineering, **118**, p 1.
[38] Vaz G., Jaouen F.A.P. & Hoekstra M.; 2009, "Free-Surface Viscous Flow Computations. Validation of URANS code FRESCO," 28th Int. Conf. on Ocean, Offshore and Arctic Engineering (OMAE), OMAE2009-79398, Honolulu, Hawaii.
[39] Menter F.R., Kuntz M. & Langtry R.; 2003, "Ten Years of Industrial Experience with the SST Turbulence Model", Turbulence, Heat and Mass Transfer, **4**, p 625.
[40] Eliasson P.; 2002, "Edge, a Navier-Stokes Solver for Unstructured Grids", In Finite Volumes for Complex Applications III, p. 527.
[41] Peng S.-H.; 2005, "Hybrid RANS-LES Modeling based on Zero and One Equation Models for Turbulent Flow Simulations", 4th Int. Symp. On Turb. Shear Flow Phen., **3**, p 1159, Williamsburg, USA.
[42] Smagorinsky J.; 1963, "General Circulation Experiments with the Primitive Equations. I. The Basic Experiment", Month. Wea. Rev., **91**, p 91.
[43] Weller H., Tabor G., Jasak H. & Fureby C.; 1998, "A Tensorial Approach to Computational Continuum Mechanics using Object Orientated Techniques", Computers in Physics, **12**, p 620.
[44] Bensow R. & Fureby C.; 2007, "On the Justification and Extension of Mixed Models in LES", J. Turb., 8 N54, p 1.
[45] Joubert P.N.; 2004, "Some Aspects of Submarine Design Part 1 – Hydrodynamics", DSTO Report DSTO-TR-1622, Melbourne, Australia.
[46] Joubert P.N.; 2004, "Some Aspects of Submarine Design Part 2 – Shape of a Submarine 2026", DSTO Report DSTO-TR-1920, Melbourne, Australia.
[47] Anderson B., Chapuis M., Erm L., Fureby C., Giacobello M., Henbest S., Jones D., Jones M., Kumar C., Liefvendahl M., Manovski P., Norrison D., Quick H., Snowden A., Valiyff A., Widjaja R. & Woodyatt B.; 2012, "Experimental and Computational Investigation of a Generic Conventional Submarine Hull Form", 29th Symposium on Naval Hydrodynamics, Gothenburg, Sweden.
[48] Fureby C., Anderson B., Clarke D., Erm L., Henbest S., Giacobello M., Jones D., Nguyen M., Johansson M., Jones M., Kumar C., Lee S-K, Manovski P., Norrison D., Petterson K., Seil G., Woodyatt B. & Zhu S.; 2015, "Experimental and Numerical Study of a Generic Conventional Submarine at 10 Yaw", Ocean Engineering, **116**, p 1.
[49] Kumar C., Manovski P. & Giacobello M.; 2012, "Particle Image Velocimetry Measurements on a Generic Submarine Hull Form. Proc. 18th Australasian Fluid Mechanics Conference, paper 188, Launceston, Tasmania, Australia.
[50] Norrison D., Petterson K., Johansson M., Liefendahl M., Anderson B. & Clarke D.; 2016, "Numerical Study of a Self-Propelled Conventional Submarine", 31st Symp. on Naval Hydrodynamics, Monteray, USA.
[51] Boussinesq J.; 1897, "Theorie de l'écoulement tourbillonnant et tumultueux des liquides dans les lits rectilignes a grande section", Gauthier-Villars et fils, Paris, France.
[52] Wilcox D.C.; 2000, "Turbulence Modelling for CFD", 2nd Ed., DCW Industries.
[53] Jones W.P. & Launder B.E.; 1972, "The Prediction of Laminarization with a Two-Equation Model of Turbulence", Int. J. Heat and Mass Transfer, **15**, p 301.
[54] Speziale C.G.; 1998, "Turbulence Modeling for Time-Dependent RANS and VLES: A Review", AIAA J., **36**, p 173.
[55] Spalart P.R. & Allmaras S.R.; 1992, "A One-Equation Turbulence Model for Aerodynamic Flows", AIAA, 92-0439.
[56] Klebanoff P.S.; 1955, "Characteristics of Turbulence in a Boundary Layer with Zero Pressure Gradient", NACA TR-1247.
[57] Jimenez J.; 2013, "Near Wall Turbulence", Phys. Fluids, **25**, p 101302.
[58] Lee M. & Moser R.D.; 2015, "Direct Numerical Simulation of Turbulent Channel Flow up to $Re_\tau \approx 5200$", J. Fluid Mech., **774**, p 395.
[59] Spalding D.B.; 1961, "A Single Formula for the Law of the Wall", Trans. ASME, J. Appl. Mech. **28**, p 455.
[60] Hoyas S. & Jiménez J.; 2008, "Reynolds Number Effects on the Reynolds-stress Budgets in Turbulent

Channels", Phys. Fluids, **20**, p 101511.
[61] Balaras E., Benocci C. & Piomelli U.; 1996, "Two-Layer Approximate Boundary Conditions for Large Eddy Simulations", AIAA J., **34**, p 1111.
[62] Kawai S. & Larsson J.; 2013, "Dynamic Non-Equilibrium Wall-Modeling for Large Eddy Simulation at High Reynolds Numbers", Phys. Fluids, **25**, p 015105.
[63] Fureby C.; 2007, "On LES and DES of Wall Bounded Flows", Ercoftac Bulletin No 72, Marsh Issue.
[64] Chin C. Ng H.C.N., Blackburn H.M, Monty J.P. & Ooi A.; 2015, "Turbulent Pipe Flow at Ret≈1000: A Comparison of Wall-Resolved Large Eddy Simulation, Direct Numerical Simulation and Hot-Wire Experiment", Comp. Fluids, **122**, p 26.
[65] Keating A. & Piomelli U.; 2006, "A Dynamic Stochastic Forcing Method as a Wall-Layer Model for Large-Eddy Simulation" J. Turb. 7, p N12.
[66] Kim J., Moin P. & Moser R.; 1987, "Turbulence Statistics in Fully Developed Channel Flow at Low Reynolds Number", J. Fluid Mech., **177**, p 133.
[67] Wosnik M., Castillo L. & George W.K.; 2000, "A Theory for Turbulent Pipe and Channel Flows", J. Fluid Mech., **421**, p 115.
[68] Kremer F. & Bogey C.; 2015, "Large-Eddy Simulation of Turbulent Channel Flow using Relaxation Filtering: Resolution Requirement and Reynolds Number Effects", Comp. Fluids, **116**, p 17.
[69] Monty J.P., Hutchins N., Ng H.C.N., Marusic I. & Chong M.S.; "A Comparison of Turbulent Pipe, Channel and Boundary Layer Flows", J. Fluid Mech., **632**, p 431.
[70] Coles D.E.; 1962, "The Turbulent Boundary Layer in a Compressible Fluid", R 403-PR, The RAND Corporation, Santa Monica, CA
[71] Fernholz H.H. & Finley P.J.; 1996, "The Incompressible Zero-Pressure-Gradient Turbulent Boundary Layer: An Assessment of the Data", Prog. Aerospace Sci. **32**, p 245.
[72] DeGraaff D.B. & Eaton J.K.; 2000, "Reynolds-Number Scaling of the Flat-Plate Turbulent Boundary Layer", J. Fluid Mech., **422**, p 319.
[73] Spalart P. R.; 1988, "Direct Simulation of a Turbulent Boundary Layer up to Re_θ=1410", J. Fluid Mech. **187**, p 61.
[74] Schlatter P. & Örlü R.; 2010, "Assessment of Direct Numerical Simulation Data of Turbulent Boundary Layers", J. Fluid Mech., **659**, p 116.
[75] Inoue M., Mathis R., Marusic I. & Pullin D.I.; 2012, "Inner-layer Intensities for the Flat-Plate Turbulent Boundary Layer Combining a Predictive Wall-Model with Large-Eddy Simulations", Phys. Fluids **24**, 075102.
[76] Hickel S. & Adams N.A.; 2008, "Implicit LES Applied to Zero-Pressure-Gradient and Adverse-Pressure-Gradient Boundary-Layer Turbulence", Int. J. Heat Fluid Flow, **29**, p 626.
[77] Ashurst W.T., Kerstein A.R., Kerr R.M. & Gibson C.H.; 1987, "Alignment of Vorticity of Scalar Gradients with Strain Rate in Simulated Navier–Stokes Turbulence", Phys. Fluids, **30**, 2343.
[78] Byun G. Simpson R.L. & Long C.H.; 2004, "Study of Vortical Separation from Three-Dimensional Symmetric Bumps", AIAA J., **42**, p 754.
[79] Byun G. & Simpson R.L.; 2005, "Structure of Three-Dimensional Separated Flow on a Axisymmetric Bump", AIAA J., **44**, p 999.
[80] Ma R. & Simpson R. L.; 2005, "Characterization of Turbulent Flow Downstream of a Three-Dimensional Axisymmetric Bump. Turb. Shear Flow Phen. 5, Williamsburg, Virginia, p. 1171.
[81] Patel N. & Menon S.; 2003, "Large-Eddy Simulation of Turbulent Flow over an Axisymmetric Hill", AIAA 2003-0967.
[82] Persson T. M. Liefvendahl, Bensow R. & Fureby C., 2005, "Numerical Investigation of the Flow over an Axisymmetric Hill using LES, DES and RANS", J. Turbulence, **7**, 4.
[83] Visbal M.R., Rizzetta D.P. & Mathew, J.; 2007, "Large-Eddy Simulation of Turbulent Flow Past a 3D Bump", AIAA 2007-0917.
[84] Garcia-Villalba M., Lin N., Rodi W. & Leschzinger M.; 2009, "Large-Eddy Simulation of Separated Flow over a Three-Dimensional Axisymmetric Hill", J. Fluid Mech., **627**, p 55.
[85] Davidson L.; 2005, "3D Low Hill with Complex Separation", in FLOMANIA: Flow-Physics Modeling – An Integrated Approach, Eds. Haase W., Aupoix B., Bunge U. & Schwamborn D., Note on Numerical Fluid

Mechanics and Multidisciplinary Design, Springer Verlag.
[86] Erm L.P.; 2003, "Calibration of the Flow in the Extended Test Section of the Low-Speed Wind Tunnel at DSTO, DSTO Report DSTO-TR-1384, Melbourne, Australia.
[87] Preston J.; 1954, "The Determination of Turbulent Skin Friction by Means of Pitot Tubes", J. Royal Aero. Soc., **58**, p 109.
[88] Gungor A.G. & Menon S.; 2010, "A New Two-Scale Model for Large Eddy Simulation of Wall-Bounded Flows", Prog. In Aerospace Sci., **46**, p 28.